Structure and composition of linear TiO_x nanostructures on $SrTiO_3(001)$

Matthew S. J. Marshall,[1,*] Andres E. Becerra-Toledo,[2] David J. Payne,[3] Russell G. Egdell,[3] Laurence D. Marks,[2] and Martin R. Castell[1,†]

[1]*Department of Materials, University of Oxford, Oxford, United Kingdom, OX1 3PH*

[2]*Department of Materials Science and Engineering, Northwestern University, Evanston, Illinois 60208, USA*

[3]*Department of Chemistry, University of Oxford, Oxford, United Kingdom, OX1 3LZ*

(Received 19 March 2012; revised manuscript received 15 July 2012; published 10 September 2012)

High-resolution x-ray photoelectron spectroscopy (XPS) was performed on the surface of 0.7 at.% Nb-doped $SrTiO_3(001)$ decorated with self-assembled linear nanostructures termed dilines, trilines, and tetralines. All three nanoline types share a common side-row feature, while the triline is shown to contain Ti in the $2+$ oxidation state as a structural component of the linear backbone. Atomic-resolution scanning tunneling microscopy images and models developed using density functional theory are used to relate the structures to the spectroscopic data, showing that the nanolines consist of a three-layer hill and valley-type structure. Valence band XPS reveals the presence of a well-defined mid-band-gap state at approximately 1 eV, which emerges as a result of nanoline formation.

DOI: 10.1103/PhysRevB.86.125416 PACS number(s): 68.35.Dv, 68.37.Ef

I. INTRODUCTION

Our understanding has evolved over the last decade towards understanding the surface structure of the prototypical perovskite oxide $SrTiO_3(001)$.[1–4] A major development was work showing that the (2×1) reconstructed surface is terminated by a double layer of TiO_2.[1] Further advances have been made in determining the structure of the reconstructed $SrTiO_3(001)$ surface.[5–9] More recently, the link between the TiO_2-terminated $c(4 \times 2)$ surface reconstruction and the nanostructured surfaces of $SrTiO_3$ was revealed.[10] The constituent unit of the $c(4 \times 2)$ reconstruction consists of four Ti atoms and eight oxygen atoms,[11] and scanning tunneling microscopy (STM) simulations of this structure resolved a long-standing difference between the structure of the $c(4 \times 2)$ reconstruction and its appearance in experimental STM images.[10–12] The $c(4 \times 2)$ structural unit also forms the basis for the spots that comprise the outer rows of the linear nanostructures.[10,13] It thereby provides a theoretical understanding of the evolution of a reconstructed surface into a nanostructured surface consisting of ordered nanolines, all composed of the same fundamental building block.

There are three types of nanoline structures that form on the surface of $SrTiO_3(001)$: dilines, trilines, and tetralines. All of the nanolines consist of parallel rows which self-assemble into domains that are oriented in the $\langle 001 \rangle$ directions.[14] Dilines were first observed nucleating on the $c(4 \times 2)$ reconstructed surface of $SrTiO_3(001)$ following a sample preparation procedure consisting of Ar^+ bombardment followed by ultrahigh vacuum (UHV) annealing at 750–975 °C.[15] A subsequent anneal at 1235 °C caused the disappearance of the dilines. High-temperature STM observed the nanolines *status nascendi* by taking successive STM images at temperatures of 825 °C, which showed the formation of stable nucleation centers and their subsequent growth.[16] Auger spectroscopy showed the nanoline surfaces to be TiO_x rich.[14] UHV annealing causes surface segregation, giving rise to nanoline decorated surfaces. The continuation of this process results in the formation of islands of anatase TiO_2.[17,18]

In this work, we focus on determining the chemical composition of self-assembled nanolines that decorate the surface of $SrTiO_3(001)$ using x-ray photoelectron spectroscopy (XPS). This information is combined with scanning tunneling microscopy and density functional theory (DFT) simulations to develop an understanding of the atomic and electronic structure of linear nanostructures on $SrTiO_3(001)$. These studies reveal how the different oxidation states of Ti play a role in the atomic and electronic structure of the surface region.

II. EXPERIMENT

Single-crystal epipolished $SrTiO_3(001)$ 0.7 at.% Nb-doped (PI-KEM Ltd, UK) samples that were $7.0 \times 2.0 \times 0.5$ mm in size were used. Stoichiometric $SrTiO_3$ is insulating, thus extrinsic n-type doping with Nb enables experimental analysis and preparation by rendering samples conductive. The samples were introduced into the ultrahigh vacuum preparation chamber of a scanning tunneling microscopy system (JEOL JSTM4500S) at a base pressure of 10^{-8} Pa. Nanostructured surfaces are prepared by Ar^+ sputtering followed by annealing at 800–900 °C in UHV, as described previously.[14] In the JSTM4500S, Ar^+ sputtering was performed at an energy of 1.0 kV for 10 min. Samples were annealed by resistive direct current heating. Above 750 °C, sample temperatures were measured using a Leeds and Northrup disappearing filament optical pyrometer.

All x-ray photoelectron spectra were obtained using a Scienta ESCA 300 spectrometer at the National Center for Electron Spectroscopy and Surface Analysis (NCESS) at the Daresbury Laboratory, UK. An Al Kα source produced monochromatic radiation at 1486.7 eV, while the effective energy resolution of the spectrometer was 400 meV with the incident beam at a 45° angle to the surface. The ESCA 300 has facilities for *in situ* Ar^+ bombardment and electron-beam heating. All nanostructured surfaces were prepared in the STM system, removed from vacuum, and then transferred to the ESCA 300 for analysis. Surface contamination was removed from the preprepared nanostructured surfaces prior

to obtaining spectra by heating in vacuum at approximately 700 °C. This is well below the surface formation temperature, and anion reordering should be minimal. Reheating in vacuum removed any evidence of carbon contamination or hydroxyl contamination from the XPS spectra. To check that the nanostructured surfaces are stable in air, we exposed a sample to ambient conditions, reintroduced it into the STM UHV chamber, heated it to approximately 700 °C, and then reimaged it. Following this procedure, we found that the surface was essentially unchanged. This experiment gives us sufficient confidence to state that although we have transferred samples from one UHV chamber to another, that the surfaces examined in both the STM and the XPS chambers are essentially the same, and any chemisorption would be reversible.

Density functional theory was used to model the structure using a repeated slab configuration. All DFT calculations were carried out under the augmented plane wave + local orbital (APW + lo) implementation of the full-electron-potential WIEN2K code. Muffin-tin radii of 2.40, 1.68, and 1.50 Bohr were consistently used for Sr, Ti, and O atoms, respectively, along with a min(RMT)*K_{max} of 5.5. The number of k points was fixed to a density of 64 points per 1 × 1 × 1 Brillouin zone. Every structure was allowed to relax such that all residual forces were below 0.1 eV Å. The Perdew-Burke-Ernzerhof (PBE) formulation[19] of the generalized gradient approximation (GGA) was used as the exchange-correlation function. Constant-current STM image simulations were carried out under a modified, high-bias version of the Tersoff-Hamann implementation.[10,20]

III. RESULTS

Figure 1(a) shows a representative STM image of a diline nanostructured surface. Dilines are formed by sputtering with Ar^+ for 10 min at an ion flux of 0.66 A/m^2, followed by annealing for 40–60 min at 800–880 °C in UHV. The dilines are shown in close-packed domains in Fig. 1(a). The dilines appear in STM images as two parallel rows of bright spots, as in Fig. 1(b). The inter-spot and inter-row separation corresponds to twice the lattice constant of $SrTiO_3$ (a_{SrTiO_3} = 0.3905 nm), while the spot height is approximately 0.2 nm, corresponding to half the $SrTiO_3$ lattice constant.[15] When found in close-packed domains, the dilines have a (6 × 2) periodicity. The dilines range in length from a minimum of 6 unit cells long (three spots)[16] to lengths exceeding 40 nm. Extensive DFT calculations revealed that the dilines have a hill-and-valley–type structure, and an STM simulation of the dilines in Fig. 1(c) shows good agreement with the experimental STM image in Fig. 1(b).[10] Differences in the details between simulated and experimental STM images may arise from differences in the way the physical STM tip convolves the surface structure and the way that this is achieved through image smearing in the simulation. The structure of the topmost layer of the diline, shown in Fig. 1(d), corresponds to the spots observed in the STM images. Each spot observed by STM corresponds to the convolution of the electronic states from 4 Ti atoms and 7.5 oxygen atoms. Dilines are observed in STM with the rows "in phase" and "out of phase" in equal proportions. The DFT modeled structures are only shown for the in-phase configuration. The top layer sits on top of a TiO_2 layer as shown in Fig. 1(e), which is on top of the bulk TiO_2 layer [Fig. 1(f)]. A side view of this configuration is shown in Fig. 1(g). The atomic configuration of this structure is shown overlaid over the STM image and STM simulation in

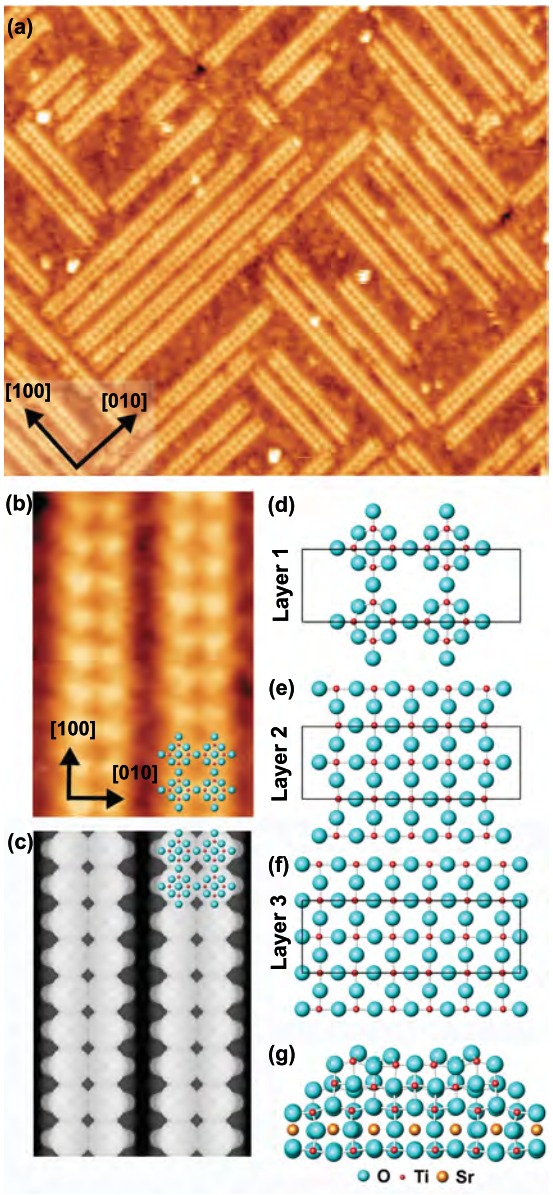

FIG. 1. (Color online) (a) A representative STM image showing a diline nanostructured surface (65.0 × 56.1 nm^2, V_s = 0.987 V, I_t = 0.200 nA). (b) A close-up of two parallel dilines, with the ball-and-stick model overlaid in the bottom right corner (7.0 × 4.7 nm^2, V_s = 0.987 V, I_t = 0.200 nA). (c) A simulated STM image of the diline image shown in (b), with the ball-and-stick model corresponding to the simulated structure shown in the upper right-hand corner (7.0 × 4.7 nm^2, V_s = 1.5 V). The ball-and-stick structures of the top three layers of a single diline nanostructure, modeled by DFT, are shown in plan view in (d)–(f). Layer 3 sits atop a bulk SrO layer. The (6 × 2) unit cell is indicated by a black rectangle. In (g), a side view of the top 5 layers of the structure, as modeled by DFT, are presented in side view. The blue spheres indicate oxygen atoms, the red spheres titanium atoms, and the gold spheres strontium atoms.

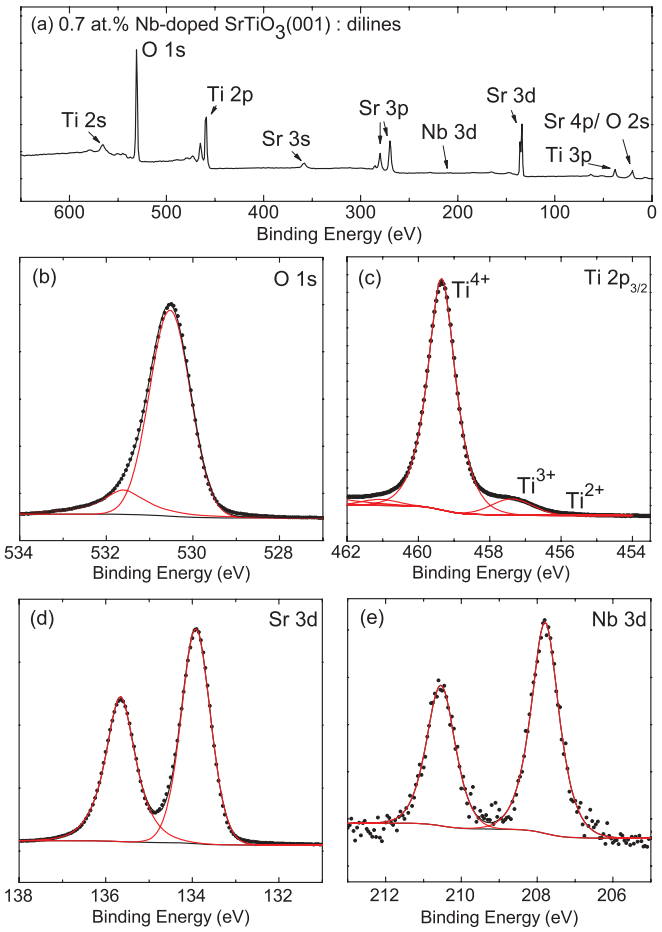

FIG. 2. (Color online) Core-level XPS spectra are presented of a representative diline nanostructured 0.7 at.% Nb-doped $SrTiO_3(001)$ sample. All nanostructured samples were prepared in the JEOL JSTM4500S, removed from UHV, and transferred into the ESCA 300 spectrometer. A survey spectrum is shown in (a). The O 1*s* peak is shown in (b). In (c), the Ti 2*p* peaks are shown, with fitted peaks corresponding to Ti in the 4+, 3+, and 2+ states corresponding to 90.5%, 8.3%, and 1.7%, respectively. The Sr 3*d* and Nb 3*d* peaks are shown in (d) and (e).

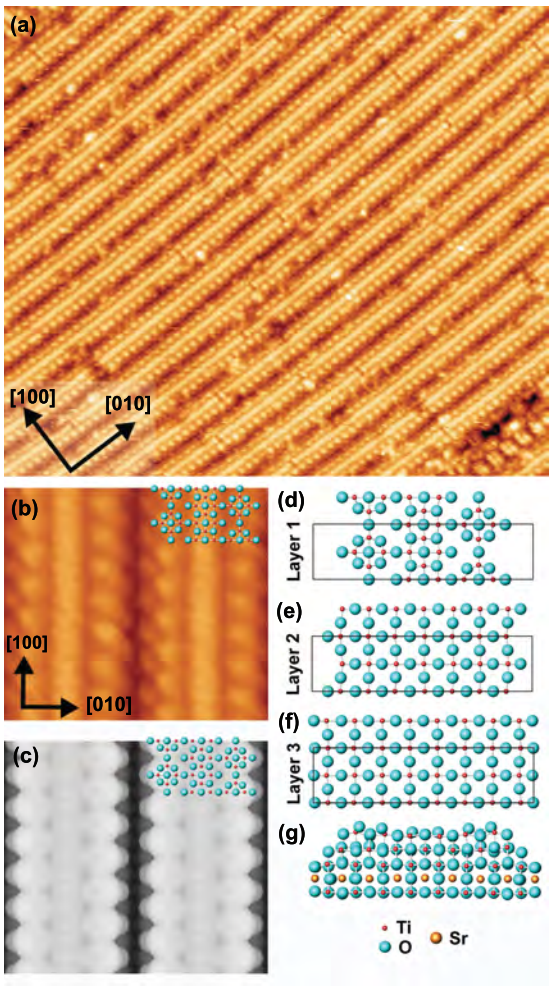

FIG. 3. (Color online) A representative STM image of a close-packed triline nanostructured surface of $SrTiO_3(001)$ is shown in (a) (55.4×47.8 nm^2, $V_s = 2.000$ V, $I_t = 0.275$ nA). A close-up image of the trilines is shown in (b) taken using high-temperature STM (6.2×5.5 nm^2, $V_s = +1.86$ V, and $I_t = 0.240$ nA at $T = 791$ K). The corresponding DFT-derived STM simulation of (b) is shown in (c) (6.2×5.5 nm^2). The ball-and-stick model of the top layer is overlaid in the top-right corners of (b) and (c). In (d)–(f), the ball-and-stick structures of the top three layers of a single triline nanostructure, modeled by DFT, are presented in plan view. The structures are shown with the side lobes in a "zigzag" configuration, where dots in each side row are out of phase by two unit cells. "Layer 3" sits atop a bulk SrO layer. An (8×2) unit cell is indicated by a black rectangle. The ball-and-stick structure of a single triline is presented in side view in (g).

the bottom-right and top-right corners of Figs. 1(b) and 1(c), respectively.

To determine the composition of the diline nanostructured surface, high-resolution XPS spectra were obtained from a representative diline nanostructured surface, shown in Fig. 2. Imaging this same surface with STM confirms that the diline nanostructures are the dominant surface feature. The O 1*s* peak, shown in Fig. 2(b), shows the emergence of a large peak at 531.5 ± 0.1 eV in addition to the primary peak at 530.5 ± 0.1 eV, both located in the same position as for an untreated sample. The Ti 2*p* spectrum shows the emergence of a small amount of Ti in the Ti^{2+} state corresponding to 1.7% of the Ti $2p_{\frac{3}{2}}$ peak areas, while the Ti^{3+} peak represents 21.1% of the total Ti $2p_{\frac{3}{2}}$ peak area. The Sr 3*d* and Nb 3*d* peaks exhibit no differences from untreated $SrTiO_3$ [Figs. 2(d) and 2(e)].

A representative STM image of a close-packed triline nanostructured surface is shown in Fig. 3(a). Trilines are formed by annealing a diline-covered surface for approximately 45 min at 890–900 °C in UHV. A close-up STM image of two triline nanostructures is shown in Fig. 3(b), and the corresponding DFT-derived STM simulation is shown in Fig. 3(c). A full discussion of the DFT performed on nanolines is described elsewhere.[10,13] The STM simulation is in excellent agreement with the experimental STM image replicating all features. The outer two rows of the triline share the same structure as the diline rows, composed of linked groups of 4 Ti atoms and 7.5 oxygen atoms, described as a polyhedral quartet motif.[10] This is the same unit that makes up the $c(4 \times 2)$ reconstruction. However, the central row of the triline nanostructure is dramatically different than the outer two rows

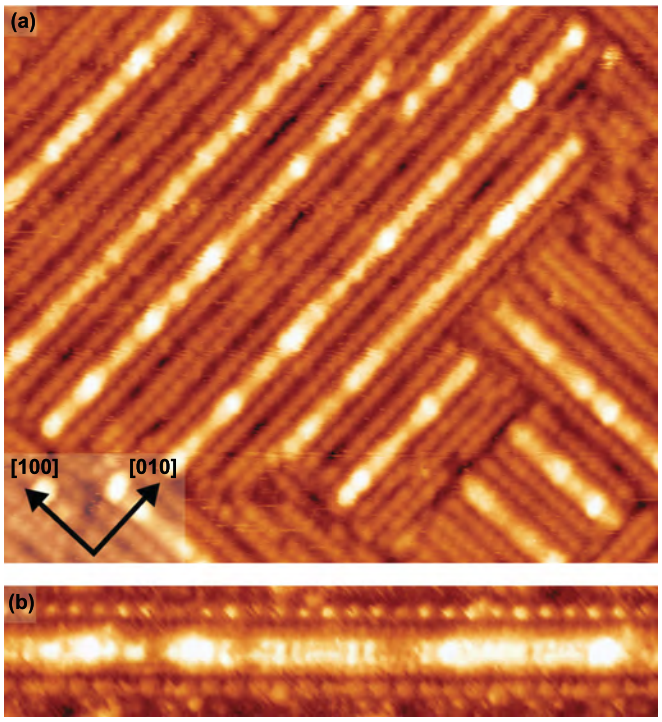

FIG. 4. (Color online) A representative STM image of a tetraline nanostructured surface is shown in (a) (44×38 nm^2, $V_s = 1.700$ V, $I_t = 0.067$ nA). A close-up image of a single tetraline, rotated 45° with respect to [010], is shown in (b) (6.0×27.3 nm^2, $V_s = 1.650$ V, $I_t = 0.070$ nA).

and consists of a TiO_x backbone with a rocksalt configuration, shown in Fig. 3(d). As with the dilines, the top layer sits on top of a TiO_2 intermediate layer shown in Fig. 3, which, in turn, sits atop the TiO_2 bulk layer, shown in Fig. 3(f). The side view of this configuration is shown in Fig. 3(g). The ball-and-stick model of the top layer of this structure is shown overlaid over the STM image and STM simulation in the top-right corners of Figs. 3(b) and 3(c), respectively. It should be noted that similar to the dilines, the side rows of the trilines are also observed in both in-phase and out-of-phase configurations in equal proportions.

A representative STM image of a tetraline nanostructured surface is shown in Fig. 4(a). A close-up image in Fig. 4(b) shows the irregular nature of the central row. Unlike the trilines, the central row of the tetralines has no discernible structure along the center of the backbone, and the appearance in STM images of the backbone is not bias dependent. Since the structure of the central row is somewhat irregular, it is not possible to extend the modeling of the dilines and trilines to the tetraline nanostructure. Based on the structure of the dilines and trilines, we speculate that the tetraline backbone may sit atop a double layer of TiO_2. Moreover, given the identical appearance of the outer rows of the nanolines, the tetraline outer rows are likely identical in structure to those of the other nanolines.

The determination of the diline and triline structures using DFT and STM is supported by using XPS to determine the surface composition. In this case, core-level XPS was performed on surfaces that were predominantly covered with dilines, trilines, or tetralines. The O 1*s*, Sr 3*d*, and Nb 3*d*

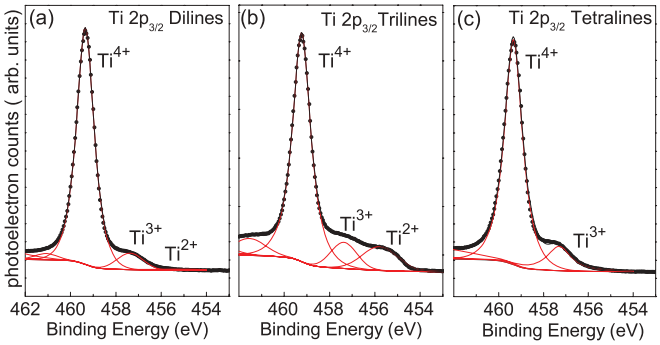

FIG. 5. (Color online) Core-level Ti $2p_{\frac{3}{2}}$ XPS spectra are shown of a representative diline nanostructured surface in (a), a triline nanostructured surface in (b), and a tetraline nanostructured surface in (c). For the dilines shown in (a), Ti^{4+} corresponds to 90.5% of the peak area, with 8.3% in the Ti^{3+} state, and 1.7% in the Ti^{2+} state. In (b), the trilines are shown to be composed of Ti^{4+} (72.5%), Ti^{3+} (19.6%), and Ti^{2+} (8.0%). In (c), the tetralines are rich in Ti^{3+} (13.6%) and Ti^{4+} (86.4%).

core-level spectra shown in Figs. 2(b), 2(d), and 2(e) for the diline nanostructured surface were unchanged for the triline and tetraline surfaces, and are consequently not included in further discussion. However, core-level XPS of the Ti $2p_{\frac{3}{2}}$ peak for each of the three linear nanostructured surfaces is markedly different. Figure 5(a) shows the Ti $2p_{\frac{3}{2}}$ peak from a diline nanostructured surface. Titanium in the 4+ state is predominant, corresponding to 90.5% of the Ti $2p_{\frac{3}{2}}$ peak areas. The Ti^{3+} peak represents 8.3% of the total Ti $2p_{\frac{3}{2}}$ peak area, and there is 1.7% of Ti in the Ti^{2+} state. The Ti $2p_{\frac{3}{2}}$ core-level binding energies are given in Table I, and are in accordance with previous studies.[21,22]

The Ti $2p_{\frac{3}{2}}$ core-level spectrum from a predominantly triline nanostructured surface is shown in Fig. 5(b). In this spectrum, 72.5% of the peak area corresponds to Ti^{4+}, 19.6% to Ti^{3+}, and 8.0% to Ti^{2+}. The emergence of a large Ti^{2+} peak is readily visible in Fig. 5(b). Core-level XPS of a representative tetraline nanostructured sample is shown in Fig. 5(c). The Ti $2p_{\frac{3}{2}}$ shows that the tetralines are rich in Ti^{4+} and Ti^{3+} (86.4% and 13.6%, respectively). Notably, the tetraline nanostructured surface, which is formed by annealing triline decorated surfaces, shows no incidence of Ti^{2+}. The core-level Ti $2p_{\frac{3}{2}}$ binding energies for the triline and tetraline decorated surfaces are given in Table I. The percentages of the peak areas for all three nanoline surfaces are summarized in Table II.

Valence band spectra were obtained from undoped, Ar^+ sputtered, and nanostructured samples. The full valence band spectra are shown in the left-hand box of Fig. 6, while close-ups

TABLE I. Core-level XPS Ti $2p_{\frac{3}{2}}$ binding energies in eV (±0.1 eV).

Surface	Ti^{4+} (eV)	Ti^{3+} (eV)	Ti^{2+} (eV)
Dilines	459.4	457.4	455.3
Trilines	459.2	457.4	455.8
Tetralines	459.3	457.3	

TABLE II. Percentage of the total Ti $2p_{\frac{3}{2}}$ core-level peak area.

Surface	% of Ti^{4+}	% of Ti^{3+}	% of Ti^{2+}
Dilines	90.5	8.3	1.7
Trilines	72.5	19.6	8.0
Tetralines	86.4	13.6	0

of the band-gap region are shown in the right-hand box of Fig. 6. The spectra were normalized such that the maxima at approximately 7 eV were equal to 1000 counts. Noisier spectra, such as Figs. 6(a), 6(b), and 6(d), correspond to fewer total scans. The "as-received" sample in Fig. 6(a) shows no evidence of mid-band-gap states. The "flashed" sample shown in Fig. 6(b), which was heated in vacuum to remove contamination, has a broad poorly defined peak, while the "sputtered" sample in Fig. 6(c) has no mid-band-gap peak, but shows a broad increase in the density of states throughout the band gap. The three nanostructured samples, shown in Figs. 6(d)–6(f), show a well-defined peak in the mid-band-gap region centered at approximately 1 eV, compared to the unstructured nature of the mid-band-gap states in Figs. 6(b) and 6(c).

Density-of-states plots, shown in Fig. 7, are computed using DFT for comparison with experimental valence band spectra. The bulk band gap was calculated to be 2.2 eV, which is smaller than the experimental band gap of 3.2 eV. Underestimation of the band gap is a well-known feature of the GGA PBE calculations performed in this paper. For comparison, the DOS from a $c(4 \times 2)$ reconstructed surface is also shown, and exhibits no mid-band-gap states. The density-of-states plots for the dilines and trilines each exhibit band-gap states, reproducing features from the valence spectra shown in Fig. 6.

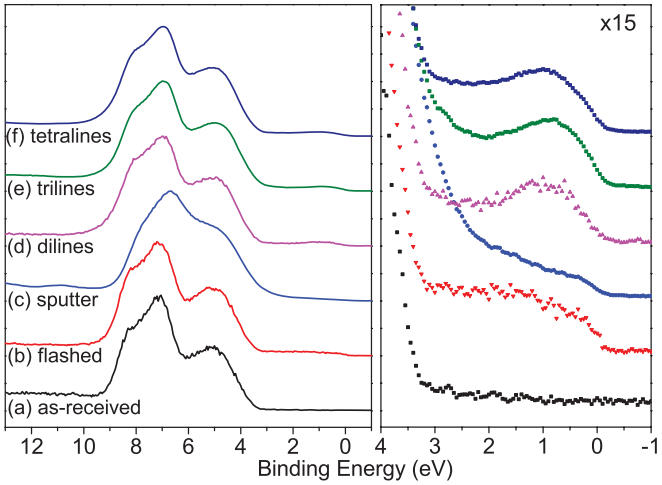

FIG. 6. (Color online) Valence band spectra taken from $SrTiO_3(001)$ following various surface treatments. The valence band spectrum of undoped-$SrTiO_3(001)$ is shown in (a), and the spectrum obtained after flashing in UHV for 7 min at 800 °C is shown in (b). The results of Ar^+ sputtering for 20 min are shown in (c). Valence band spectra corresponding to the dilines, trilines, and tetralines are shown in (d), (e), and (f), respectively. The left-hand panel shows the complete valence and band-gap regions of the spectra, while the right-hand panel shows magnified regions of each spectrum in the band-gap region.

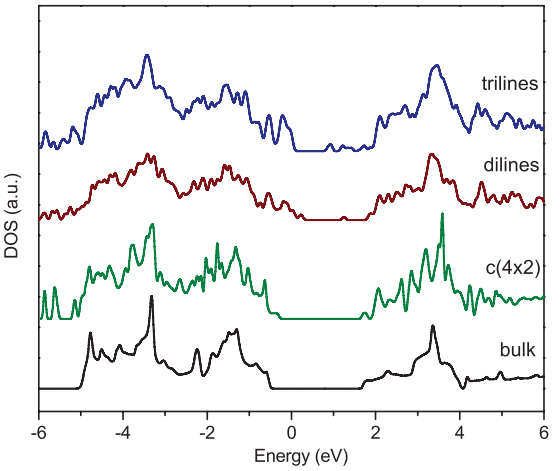

FIG. 7. (Color online) Density of states calculated with DFT for trilines, dilines, a $c(4 \times 2)$ surface and the bulk. All spectra are normalized to the O 1*s* peak and plotted with respect to the bulk Fermi energy. The trilines and diline spectra are each averages of the zigzag and in-plane structures.

The dilines and trilines DOS are averages of the structures in the zigzag and square configurations (such that the outer side rows are either in phase or out of phase).

IV. DISCUSSION

In Fig. 1, the diline is depicted in STM images, and theoretically derived simulations, with excellent agreement between theory and experiment. The notable feature in Fig. 1(d) is that the constituent unit of the diline rows shares the structure of the polyhedral quartet motif that causes the appearance of the $c(4 \times 2)$ reconstruction.[10] This links the structure of the TiO_x-rich reconstructions to that of the nanolines, which all share a stable common structural motif in the outer rows, as can be seen in Figs. 1, 3, and 4.

In Fig. 3, the triline backbone (central row) is the feature which differentiates trilines from dilines and tetralines. The prevalence of Ti^{2+} in XPS spectra obtained from the triline nanostructured surface therefore implies that the Ti^{2+} is, more specifically, a structural feature of the triline backbone rather than the result of electronic doping. The presence of Ti^{2+} as a structural feature of the triline reveals an important aspect of the triline structure. The two parallel side lobes of the triline are identical to the diline and tetraline side lobes, neither of which exhibit Ti^{2+}. Ti^{2+} is not introduced as a result of UHV annealing, or Ar^+ ion bombardment, or Nb doping.[23] There are a limited number of atomic configurations of the triline backbone that can realistically explain the observed STM images of the surface, as well as the XPS spectrum shown in Fig. 5(b). DFT simulations were performed on numerous possible structures, with the final structure showing excellent agreement between theory and experiment. Taking the XPS in conjunction with the STM and DFT indicates that the triline backbone contains a large fraction of Ti in the 2+ state.

One might expect that the tetralines would contain more reduced Ti than the trilines since they are annealed in UHV for

a longer period of time; this is not reflected in the XPS spectra shown in Fig. 5(c). The XPS spectra shown in Fig. 5(c) show that the tetralines contain no Ti in the Ti^{2+} state, and less Ti in the $3+$ state than the trilines. Since annealing nanostructured surfaces can result in the formation of islands of anatase, we speculate that the central row of the tetraline contains TiO_2. In the case of the tetraline in Fig. 4, the observed irregularity in the central row of the tetraline makes any attempt at simulating its structure difficult.

The valence band spectra shown in Fig. 6 show that the formation of linear nanostructures on the surface of $SrTiO_3(001)$ is accompanied by the formation of a well-defined mid-band-gap state. Mid-band-gap states in Ar^+ sputtered $SrTiO_3$ were found to give rise to emission of blue light,[24] which suggests that the optical properties of the nanolines merit further investigation. This mid-band-gap state therefore appears to be related to the structure of the nanolines.[25–27] Calculations of the density of states with DFT showing band-gap states are in agreement with the XPS spectra. Notably, while the DOS plot of the $c(4 \times 2)$ structure in Fig. 7 shares many structural features with the nanolines,[10] there is an absence of band-gap states in the DOS. This difference between the $c(4 \times 2)$ and nanolines is consistent with our supposition that mid-band-gap states are uniquely associated with the nanolines.

V. CONCLUSION

Our studies of the self-assembled nanostructured surfaces of $SrTiO_3(001)$ provide spectroscopic evidence supporting structural models of the TiO_2-rich nanostructured surfaces, and showing the emergence of a mid-band-gap state. This work provides us a very comprehensive understanding of a TiO_2-terminated surface that exists independent of a TiO_2 bulk crystal. There are many practical applications for TiO_2, for instance, photocatalysis and solar energy conversion.[28,29] $SrTiO_3$ stabilizes a different form of TiO_2 on the surface, and is technologically relevant since it is one of the few materials that can be integrated with silicon.[30]

ACKNOWLEDGMENTS

The authors thank C. Spencer of JEOL UK and D. Law at NCESS for valuable technical support and assistance. M.S.J.M. thanks JEOL UK for funding. A.E.B. and L.D.M. acknowledge support by the National Science Foundation on Grant No. DMR 0906306.

*Current address: CRISP, Department of Applied Physics, Yale University, Connecticut.
†martin.castell@materials.ox.ac.uk

[1] N. Erdman, K. R. Poeppelmeier, M. Asta, O. Warschkow, D. E. Ellis, and L. D. Marks, Nature (London) **419**, 55 (2002).
[2] N. Erdman, O. Warschkow, M. Asta, K. R. Poeppelmeier, D. E. Ellis, and L. D. Marks, J. Am. Chem. Soc. **125**, 10050 (2003).
[3] R. I. Eglitis and D. Vanderbilt, Phys. Rev. B **77**, 195408 (2008).
[4] A. Biswas, P. B. Rossen, C.-H. Yang, W. Siemons, M.-H. Jung, I. K. Yang, R. Ramesh, and Y. H. Jeong, Appl. Phys. Lett. **98**, 051904 (2011).
[5] R. Herger, P. R. Willmott, O. Bunk, C. M. Schleputz, B. D. Patterson, and B. Delley, Phys. Rev. Lett. **98**, 076102 (2007).
[6] T. Kubo and H. Nozoye, Phys. Rev. Lett. **86**, 1801 (2001).
[7] L. M. Liborio, C. G. Sanchez, A. T. Paxton, and M. W. Finnis, J. Phys.: Condens. Matter **17**, L223 (2005).
[8] D. T. Newell, A. Harrison, F. Silly, and M. R. Castell, Phys. Rev. B **75**, 205429 (2007).
[9] K. Johnston, M. R. Castell, A. T. Paxton, and M. W. Finnis, Phys. Rev. B **70**, 085415 (2004).
[10] A. E. Becerra-Toledo, M. S. J. Marshall, M. R. Castell, and L. D. Marks, J. Chem. Phys. **136**, 214701 (2012).
[11] O. Warschkow, M. Asta, N. Erdman, K. R. Poeppelmeier, D. E. Ellis, and L. D. Marks, Surf. Sci. **573**, 446 (2004).
[12] M. R. Castell, Surf. Sci. **505**, 1 (2002).
[13] M. S. J. Marshall, A. E. Becerra-Toledo, L. D. Marks, and M. R. Castell, Phys. Rev. Lett. **107**, 086102 (2011).
[14] D. S. Deak, F. Silly, D. T. Newell, and M. R. Castell, J. Phys. Chem. B **110**, 9246 (2006).
[15] M. R. Castell, Surf. Sci. **516**, 33 (2002).
[16] H. L. Marsh, D. S. Deak, F. Silly, A. I. Kirkland, and M. R. Castell, Nanotechnology **17**, 3543 (2006).
[17] M. S. J. Marshall and M. R. Castell, Phys. Rev. Lett. **102**, 146102 (2009).
[18] F. Silly and M. R. Castell, Appl. Phys. Lett. **85**, 3223 (2004).
[19] J. P. Perdew, K. Burke, and M. Ernzerhof, Phys. Rev. Lett. **77**, 3865 (1996).
[20] J. Tersoff and D. R. Hamann, Phys. Rev. Lett. **50**, 1998 (1983).
[21] D. Morris, Y. Dou, J. Rebane, C. E. J. Mitchell, R. G. Egdell, D. S. L. Law, A. Vittadini, and M. Casarin, Phys. Rev. B **61**, 13445 (2000).
[22] S. Bartkowski, M. Neumann, E. Z. Kurmaev, V. V. Fedorenko, S. N. Shamin, V. M. Cherkashenko, S. N. Nemnonov, A. Winiarski, and D. C. Rubie, Phys. Rev. B **56**, 10656 (1997).
[23] M. S. J. Marshall, D. T. Newell, D. J. Payne, R. G. Egdell, and M. R. Castell, Phys. Rev. B **83**, 035410 (2011).
[24] D. Kan *et al.*, Nat. Mater. **4**, 816 (2005).
[25] M. Nakamura, T. Yoshida, K. Mamiya, A. Fujimori, Y. Taguchi, and Y. Tokura, Mater. Sci. Eng. B. **68**, 123 (1999).
[26] M. Takizawa *et al.*, Phys. Rev. Lett. **97**, 057601 (2006).
[27] W. Siemons, G. Koster, A. Vailionis, H. Yamamoto, D. H. A. Blank, and M. R. Beasley, Phys. Rev. B **76**, 075126 (2007).
[28] A. Fujishima, X. Zhang, and D. A. Tryk, Surf. Sci. Rep. **63**, 515 (2008).
[29] B. O'Regan and M. Graetzel, Nature (London) **353**, 737 (1991).
[30] J. W. Reiner, A. M. Kolpak, Y. Segal, K. F. Garrity, S. Ismail-Beigi, C. H. Ahn, and F. J. Walker, Adv. Mater. (Weinheim, Ger.) **22**, 2919 (2010).